

# Total Variation Regularized Reweighted Sparse Nonnegative Matrix Factorization for Hyperspectral Unmixing

Wei He, *Student Member, IEEE*, Hongyan Zhang, *Senior Member, IEEE*,  
and Liangpei Zhang, *Senior Member, IEEE*

**Abstract**—Blind hyperspectral unmixing (HU), which includes the estimation of endmembers and their corresponding fractional abundances, is an important task for hyperspectral analysis. Recently, nonnegative matrix factorization (NMF) and its extensions have been widely used in HU. Unfortunately, most of the NMF-based methods can easily lead to an unsuitable solution, due to the nonconvexity of the NMF model and the influence of noise. To overcome this limitation, we make the best use of the structure of the abundance maps, and propose a new blind HU method named total variation regularized reweighted sparse NMF (TV-RSNMF). First, the abundance matrix is assumed to be sparse, and a weighted sparse regularizer is incorporated into the NMF model. The weights of the weighted sparse regularizer are adaptively updated related to the abundance matrix. Second, the abundance map corresponding to a single fixed endmember should be piecewise smooth. Therefore, the TV regularizer is adopted to capture the piecewise smooth structure of each abundance map. In our multiplicative iterative solution to the proposed TV-RSNMF model, the TV regularizer can be regarded as an abundance map denoising procedure, which improves the robustness of TV-RSNMF to noise. A number of experiments were conducted in both simulated and real-data conditions to illustrate the advantage of the proposed TV-RSNMF method for blind HU.

**Index Terms**—Blind unmixing, hyperspectral image, nonnegative matrix factorization (NMF), reweighted sparsity, total variation (TV).

## I. INTRODUCTION

**H**YPERSPECTRAL image (HSI) analysis has matured into one of the most powerful and fastest-growing technologies in the field of remote sensing. The hyperspectral data provide contiguous or noncontiguous 10-nm bands throughout

the 300–2500-nm region of the electromagnetic spectrum [1]. With the wealth of available spectral information, hyperspectral imagery has been found to be very useful for many remote sensing applications [2]–[7]. Unfortunately, due to the limitation of the spatial resolution and the complexity of the terrain, a single pixel may contain several kinds of substances, and is called a “mixed pixel” [8], [9]. Mixed pixels are common in HSIs, and severely degrade the application of hyperspectral data. In order to make full use of hyperspectral data, hyperspectral unmixing (HU) has become an essential procedure for HSI analysis.

The purpose of HU is to decompose a mixed pixel into a collection of constitute spectra, called endmembers, and their corresponding proportions, named abundances. HU algorithms mainly rely on the expected type of mixing, which can be characterized as either a linear or nonlinear model [1]. The nonlinear mixing model describes the mixed spectrum by assuming that the observed pixel is generated from a nonlinear function of the abundances associated with the endmembers [10]. However, in a real HSI scene, a small highly reflective material is capable of dominating the reflectance of a larger less reflective material at a given pixel [11]. Despite this fact and other nonlinear properties in HSIs, more and more researchers have centralized their HU work based on the linear mixing model (LMM) in recent years, since the LMM is generally recognized as an acceptable model for many real-world scenarios.

The LMM assumes that the different endmembers do not interfere with each other. Based on the LMM, many conventional HU algorithms have been proposed, e.g., endmember determination plus inversion [12]–[15], dictionary-based sparse regression [16]–[18], and statistical approaches [19]. In this paper, we focus on the nonnegative matrix factorization (NMF) [20] based approaches to HU. NMF tries to decompose the high-dimensional data into the multiplication of two nonnegative matrices: one consisting of “basis vectors” and the other containing “coefficient vectors” [21]. NMF is an attractive model that has been widely applied to HU [22]. Unfortunately, the solution space of NMF is very large if no further constraints are taken into consideration. In addition, due to the nonconvexity of the objective function of NMF, the algorithm may fall into local minima. To alleviate this situation, the abundance sum-to-one constraint (ASC)

Manuscript received February 2, 2016; revised June 6, 2016 and December 12, 2016; accepted March 14, 2017. This work was supported in part by the National Natural Science Foundation of China under Grant 41571362, Grant 61261130587, and Grant 41431175, in part by the Fundamental Research Funds for Central Universities under Grant 2015904020202, and Grant 2042017kf0218 and in part by the Major Special Project of the China High Resolution Earth Observation System. (Corresponding author: Hongyan Zhang.)

The authors are with the State Key Laboratory of Information Engineering in Surveying, Mapping and Remote Sensing, and the Collaborative Innovation Center of Geospatial Technology, Wuhan University, Wuhan 430079, China (e-mail: weihe1990@whu.edu.cn; zhanghongyan@whu.edu.cn; zlp62@whu.edu.cn).

Color versions of one or more of the figures in this paper are available online at <http://ieeexplore.ieee.org>.

Digital Object Identifier 10.1109/TGRS.2017.2683719

was first added to constrain the solution space. To further shrink the solution space, additional constraints have also been imposed upon the endmembers. Miao and Qi [23] integrated the simplex volume minimization constraint into the NMF model, and proposed the minimum volume constrained NMF approach for HU. Huck *et al.* [24] assumed that the solution to the endmember spectra should have minimum variance, and proposed minimum dispersion constrained NMF to unmix HSIs. Wang *et al.* [25] proposed the endmember dissimilarity constrained NMF method. Wang *et al.* [25] assumed that the endmember signal should itself be smooth, which is an approach that was also adopted in [11].

Another strategy to shrink the solution space is adding the constraint to the abundance maps in the NMF model. Generally, two kinds of priors are considered in constraining the abundance matrix. First, the column of the abundance matrix (corresponding to the coefficient of a single fixed pixel under the endmember dictionary) should be sparse. This is mainly because most pixels in HSIs are mixed by a subset of endmembers, rather than all the endmembers. Under this assumption, sparse coding [26] was first introduced into HU to measure the sparseness of the abundance. In [27], the S-measure constraint was used to measure the sparsity of the abundance. To overcome the defect of the  $L_1$  regularizer, in that it does not enforce the full additivity constraint, Qian *et al.* [28] also explored the use of the  $L_{1/2}$  regularizer to restrict the sparseness of the abundance maps. Compared to the  $L_1$  regularizer, the  $L_{1/2}$  regularizer can not only provide sparse solutions which are closer to the truth, but is also computationally efficient. In [11], the  $L_q$  regularizer was considered to further promote the sparse unmixing of HSIs. The  $L_q$  regularizer can be regarded as an extension of the  $L_{1/2}$  regularizer, and Sigurdsson *et al.* [11] pointed out that the  $L_q$  regularizer can outperform the  $L_1$  regularizer when the signal-to-noise ratio (SNR) is low or the sparsity of the underlying model is high. However, how to adaptively select the value of  $q$  is a key problem. Zhu *et al.* [29] focused on this issue and proposed a data-guided method to fix the value of  $q$ .

Second, the row of the abundance matrix (corresponding to the abundance map related to one fixed material) should be piecewise smooth. This is due to the fact that two neighboring pixels are more likely to have similar fractional abundances for the same endmember [17]. Based on this fact, Liu *et al.* [30] proposed abundance separation and smoothness constrained NMF (ASSNMF) for HU. Liu *et al.* [31] introduced local neighborhood weights into the NMF model and obtained a more robust HU method, and it was found that the local neighborhood weights could effectively segment the homogenous and transition areas between different ground-cover types. In [32] and [33], manifold structures were embedded into the NMF model, so that highly similar neighboring pixels could be unmixed together.

In this paper, we explore the properties of the abundance maps, and we propose a new blind HU algorithm named total variation regularized reweighted sparse NMF (TV-RSNMF). From the column perspective of the abundance matrix, only a subset of the endmembers is used to generate the fixed pixel. We therefore introduce a weighted sparse regulariza-

tion to enhance the sparsity of the abundance maps in the NMF model. Typically, weighted sparse models are used in supervised learning [34]–[36] in which the dictionary is fixed. In this paper, we explore the sparsity of the abundance maps in NMF with a weighted sparse model, which is more challenging since the dictionary (the endmember matrix) is also updated along with the iteration. In addition, by using an iterative method to solve the proposed weighted sparse model, we update the weights used for the next iteration by computing from the abundance matrix of the current solution. From the row perspective of the abundance matrix, the abundance maps related to one fixed material are assumed to be piecewise smooth [37], and we adopt the TV regularizer to promote the piecewise smooth property. TV regularization can be regarded as an abundance map denoising procedure, which significantly improves the robustness of the proposed method to noise. The main contributions of this paper are summarized as follows.

- 1) The reweighted sparse regularizer is incorporated into the NMF model to promote the sparsity of the abundance maps. The reweighted sparse regularizer, which can also be interpreted as a log-sum penalty function, has the potential to be much more sparsity-encouraging than the  $L_1$  norm.
- 2) The TV regularizer is embedded into the reweighted sparse NMF model to capture the piecewise smooth structure of the abundance maps. By the use of the TV regularizer, the spatial information of the abundance maps is enhanced, and the nearby pixels of the HSI are more likely to be composited by the same materials.

The rest of this paper is organized as follows. In Section II, the background to HU is introduced. The proposed TV-RSNMF model and its corresponding optimization solution method are presented in Sections III and IV, respectively. In Section V, both simulated and real-data experiments are described and analyzed, and the conclusions are drawn in Section VI.

## II. BACKGROUND

### A. Linear Mixing Model

The LMM assumes that a pixel in a hyperspectral data set is a linear mixture of  $K$  known pure material signatures, called endmembers:  $\mathbf{A} := [a_1, a_2, \dots, a_K] \in \mathbf{R}^{L \times K}$ , in which  $a_i \in \mathbf{R}^{L \times 1}$  is the spectral signature of the  $i$ th endmember and  $L$  represents the number of HSI bands. The corresponding proportion is called the abundance and is denoted as  $\mathbf{S} := [s_1, s_2, \dots, s_N] \in \mathbf{R}^{K \times N}$ , with  $N$  representing the number of pixels of the whole HSI. Based on the LMM, the HSI data set can be expressed as

$$\mathbf{Y} = \mathbf{AS} + \mathbf{N} \quad (1)$$

where  $\mathbf{Y} \in \mathbf{R}^{L \times N}$  denotes the signature vectors corresponding to the pixels in the HSI, and  $\mathbf{N}$  represents Gaussian noise. In general, two constraints—the abundance nonnegative constraint (ANC) and the ASC—are added to restrict the LMM model, and can be explicitly given by

$$\mathbf{S} \geq 0 \quad (2)$$

$$\mathbf{1}_K^T \mathbf{S} = \mathbf{1}_N^T \quad (3)$$

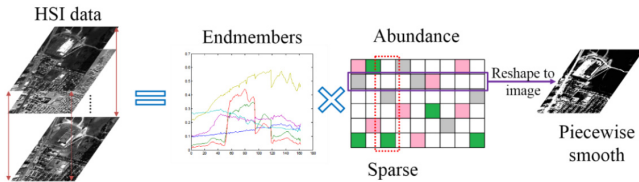


Fig. 1. Flowchart of the proposed method.

where  $\mathbf{1}_K^T$  and  $\mathbf{1}_N^T$  represent all-one vectors with size  $K$  and size  $N$ , respectively.

### B. Nonnegative Matrix Factorization

NMF has received considerable attention in the field of HU due to its many advantages. The LMM assumes that the HSI consists of spectral signatures of endmembers with corresponding nonnegative abundances. Therefore, the nonnegativity of  $\mathbf{A}$  and  $\mathbf{S}$  mentioned earlier is a natural property of the measured quantities in the hyperspectral data. The objective function of the classical NMF method is presented as follows:

$$\min_{\mathbf{A}, \mathbf{S}} \frac{1}{2} \|\mathbf{Y} - \mathbf{AS}\|_F^2, \quad \text{s.t. } \mathbf{A} \geq 0, \quad \mathbf{S} \geq 0, \quad \mathbf{1}_K^T \mathbf{S} = \mathbf{1}_N^T \quad (4)$$

where  $\|\cdot\|_F$  is the Frobenius norm of the matrix.

### III. PROPOSED TOTAL VARIATION REGULARIZED REWEIGHTED SPARSE NONNEGATIVE MATRIX FACTORIZATION MODEL

Since the objective function of the NMF model is nonconvex, a large number of minima occur during unmixing, and it is clear that the solution to the function may not be unique, which leads to instability in the unmixing. Therefore, more reasonable constraints should be added to the traditional NMF model. As presented in Fig. 1, from the column perspective, the abundance of a single fixed pixel is usually assumed to be sparse. In addition, from the row perspective of the abundance matrix, the abundance map corresponding to one fixed material is considered to be piecewise smooth. In this part, we integrate the sparseness prior and piecewise smooth regularization into the NMF model to constrain the solution space of the abundance maps, and we present the TV-RSNMF model for HU.

#### A. Reweighted Sparse Prior

As presented in Fig. 1, from the column perspective, the abundance of a single fixed pixel is usually assumed to be sparse. This is due to the fact that most of the pixels are mixtures of only a few of the endmembers in the scene [28]. A typical sparse solution can be summarized as the following  $L_0$  minimization problem:

$$\min_s \|s\|_0, \quad \text{s.t. } y = \mathbf{A}s \quad (5)$$

where  $\|s\|_0$  counts the number of nonzero components of  $s$ . Since the  $L_0$  minimization formulation is a nonconvex and

NP-hard problem, it is usually relaxed to the following  $L_1$  minimization problem:

$$\min_s \|s\|_1, \quad \text{s.t. } y = \mathbf{A}s. \quad (6)$$

Despite its wide use, the  $L_1$  regularizer cannot enforce further sparsity when the full additivity constraint of the material abundances is used [28]. As a result, many other regularizers, such as the S-measure constraint [27],  $L_{1/2}$  [28],  $L_p$  [11], and data-guided sparsity [29], have been introduced to explore the sparsity of the abundance maps. In this paper, inspired by the pursuit of sparser representation in [34], we propose to utilize a weighted sparse regularizer to enhance the sparsity of the abundance matrix in the NMF model.

Candès *et al.* [34] proved that by carefully weighting the  $L_1$  norm and iteratively updating the weights, the recovery performance of the  $L_1$  minimization framework can be greatly enhanced. The weighted  $L_1$  minimization problem can be summarized as follows:

$$\min_s \|w \odot s\|_1, \quad \text{s.t. } y = \mathbf{A}s \quad (7)$$

in which  $w \in \mathbf{R}^{K \times 1}$  is the weight vector, and operator  $\odot$  means element-wise multiplication.

We take a simple example to illustrate the difference between  $L_1$  minimization and weighted  $L_1$  minimization. Suppose  $y = \mathbf{A}s^0 = [1, 1, 2]^T$  and

$$\mathbf{A} = \begin{bmatrix} 2 & 1 & 1 \\ 1 & 1 & 2 \\ 3 & 2 & 3 \end{bmatrix}.$$

The solution of the  $L_0$  minimization (5) is then  $s^0 = [0, 1, 0]^T$ , while the  $L_1$  minimization (6) will find a different solution,  $s^0 = [1/3, 0, 1/3]^T$ . Clearly, the solution to (5) is sparser than that of (6). If we introduce a weighting vector  $w = [3, 1, 3]^T$ , the weighted  $L_1$  minimization (7) will find the solution in the same way as (5).

As in the illustration, the weighted  $L_1$  regularizer can obtain a sparser result than the  $L_1$  regularizer, under the proper weighting vector. Clearly, how to set the weighting vector to improve the sparsity of (7) is a crucial problem. Theoretically, in the weighted sparse minimization formulation (7), a larger  $w_i$  will promote the penalty magnitude of  $s_i$  to be smaller or even 0, and a smaller  $w_i$  will encourage the penalty magnitude of  $s_i$  to be larger and nonzero. As a rough rule of thumb, the value of the weight should be inversely proportional to the value of  $s$ . However, if the exact solution to  $s$  is unknown, the suitable determination of the weighted matrix is still a difficult task. Fortunately, Candès *et al.* [34] proposed an iteratively reweighted algorithm, solving a sequence of weighted  $L_1$  minimization problems, where the weights used for the next iteration are computed from the value of the current solution. In this paper, we add this weighted  $L_1$  regularizer to the NMF model, and the objective minimization is presented as follows:

$$\min_{\mathbf{A}, \mathbf{S}} \frac{1}{2} \|\mathbf{Y} - \mathbf{AS}\|_F^2 + \lambda \|\mathbf{W} \odot \mathbf{S}\|_1 \quad (8)$$

$$\text{s.t. } \mathbf{A} \geq 0, \quad \mathbf{S} \geq 0, \quad \mathbf{1}_K^T \mathbf{S} = \mathbf{1}_N^T$$

where  $W$  is the weighted matrix with nonnegative elements. As in [28], we also retain the ASC constraint. The solution to (8) is briefly presented in Algorithm 1, in which the weight matrix  $W$  used for the next iteration is computed from the abundance matrix of the current solution

$$W_{i,j}^{(k+1)} := 1/(|\mathbf{S}_{i,j}^{(k)}| + \text{eps}). \quad (9)$$

In (9),  $\mathbf{S}_{i,j}^{(k)}$  represents the abundance matrix of the  $k$ th iteration, and  $\text{eps}$  is the predetermined positive constants. As introduced in [34], the reweighted sparse model can also be interpreted as a nonconvex log-sum penalty function, and the optimization (8) can be reformulated as

$$\begin{aligned} \min_{\mathbf{A}, \mathbf{S}} \quad & \frac{1}{2} \|\mathbf{Y} - \mathbf{A}\mathbf{S}\|_F^2 + \lambda \sum_{i=1}^N \sum_{j=1}^K \log(\mathbf{S}_{i,j} + \text{eps}) \\ \text{s.t.} \quad & \mathbf{A} \geq 0, \quad \mathbf{S} \geq 0, \quad \mathbf{1}_K^T \mathbf{S} = \mathbf{1}_N^T. \end{aligned}$$

In particular, the log-sum penalty function has the potential to be much more sparsity encouraging than the  $L_1$  norm, which also indicates the superiority of the reweighted sparse model. More details of the relationship between the reweighted sparse model (8) and the log-sum penalty function can be found in [34]. From the computational perspective, by using the iterative reweighting strategy in Algorithm 1, the optimization (8) can be more easily solved by a series of convex optimization problems, and the weight matrix is updated step by step, approaching a result that is inversely proportional to the exact solution to  $\mathbf{S}$ .

---

#### Algorithm 1 Iterative Reweighted Sparse NMF (RSNMF)

---

- 1 **Input:** HSI image  $\mathbf{Y}$ ,  $\lambda$ .
  - 2 **Output:**  $\mathbf{A}$  and  $\mathbf{S}$ .
  - 3 **Initialize:**  $\mathbf{A}^{(0)}$ ,  $\mathbf{S}^{(0)}$ , and  $W^{(0)}$ .
  - 4 **Repeat until convergence**
  - 5 Update the weight matrix with (9).
  - 6 Fix  $\mathbf{S}^{(k)}$ , update  $\mathbf{A}^{(k+1)}$  via (8).
  - 7 Fix  $\mathbf{A}^{(k+1)}$ , update  $\mathbf{S}^{(k+1)}$  via (8).
- 

#### B. Total Variation Regularization

The objective minimization of RSNMF (8) can be reformulated as follows:

$$\begin{aligned} \min_{\mathbf{A}, \mathbf{S}} \quad & \sum_{j=1}^K \left( \frac{1}{2} \|\mathbf{Y}_j - \mathbf{A}\mathbf{S}_j\|_F^2 + \lambda \|\mathbf{W}_j \odot \mathbf{S}_j\|_1 \right) \\ \text{s.t.} \quad & \mathbf{A} \geq 0, \quad \mathbf{S} \geq 0, \quad \mathbf{1}_K^T \mathbf{S} = \mathbf{1}_N^T \end{aligned} \quad (10)$$

where  $W_j$  is the  $j$ th column of the weight matrix  $W$ , and  $\mathbf{S}_j$  is the abundance vector of the  $j$ th pixel. From (10), it is clear that the RSNMF model is a spectral-based HU method independently processing the HSI pixels one by one, and ignoring the spatial-contextual information of the HSI. However, as pointed out in [17] and [38], it is important to include the spatial information in HSI analysis. Fig. 2 presents a simple example demonstrating the importance of spatial information in the unmixing procedure. If only spectral information is used, situations like the one described in the figure

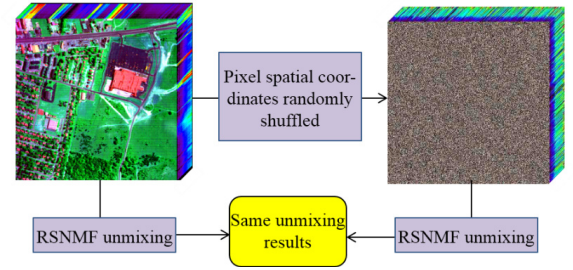


Fig. 2. Example demonstrating the importance of spatial information in HU.

may happen. Consequently, how to explore the spatial-contextual information in blind HU is a crucial problem. In this paper, we integrate the TV regularizer into the RSNMF model to promote the piecewise smooth structure of the abundance maps, as presented in Fig. 1.

Due to its ability to effectively preserve the edge information and promote piecewise smoothness, the TV model was first proposed by Rudin *et al.* [39] to solve the gray-level image denoising problem. For a gray-level image  $\mathbf{x}$  of size  $m \times n$ , the anisotropic TV norm [40] is defined as

$$\begin{aligned} \|\mathbf{x}\|_{\text{TV}} = & \sum_{i=1}^{m-1} \sum_{j=1}^{n-1} \{|x_{i,j} - x_{i+1,j}| + |x_{i,j} - x_{i,j+1}|\} \\ & + \sum_{i=1}^{m-1} |x_{i,n} - x_{i+1,n}| + \sum_{j=1}^{n-1} |x_{m,j} - x_{m,j+1}|. \end{aligned} \quad (11)$$

For an HSI, every band of the HSI is treated as a gray-level image. This gray-level TV norm can be applied to each band, respectively, and then added together. This simple band-by-band HSI TV norm is defined as follows:

$$\|\mathbf{X}\|_{\text{HTV}} = \sum_{j=1}^L \|\mathcal{F}\mathbf{X}^j\|_{\text{TV}} \quad (12)$$

in which  $\mathbf{X} = \mathbf{A}\mathbf{S} \in \mathbf{R}^{L \times N}$  is the clean image,  $\mathbf{X}^j$  represents the row vector form of the  $j$ th band of the HSI, and  $\mathcal{F}: \mathbf{R}^N \rightarrow \mathbf{R}^{m \times n}$  denotes the operator that reshapes the vector of the  $j$ th band back into the 2-D  $m \times n$  image. Here, we define  $N = m \times n$ .

After defining the TV norm of the HSI, we can treat it as a prior and incorporate it in the maximum *a priori* estimation [41] to explore the piecewise smooth structure of the abundance maps, which can be formulated as an abundance denoising model

$$\hat{\mathbf{L}} = \arg \min_{\mathbf{L} \in \mathbf{R}^{L \times N}} \left\{ \frac{1}{2} \|\mathbf{L} - \mathbf{S}\|_F^2 + \tau \|\mathbf{L}\|_{\text{HTV}} \right\} \quad (13)$$

where  $\mathbf{S}$  is the abundance matrix defined before,  $\hat{\mathbf{L}}$  denotes the denoised abundance maps, and  $\|\mathbf{L}\|_{\text{HTV}} = \sum_{j=1}^K \|\mathcal{F}\mathbf{L}^j\|_{\text{TV}}$  is the TV of the abundance maps. Significantly, compared to the input abundance maps  $\mathbf{S}$ , the output abundance maps  $\hat{\mathbf{L}}$  can obtain a more piecewise smooth structure.

#### C. TV-RSNMF HU Model

By integrating the TV regularization of the abundance maps into the RSNMF model, the objective minimization function

of the proposed TV-RSNMF model becomes

$$J(\mathbf{A}, \mathbf{S}) = \min_{\mathbf{A}, \mathbf{S}} \frac{1}{2} \|\mathbf{Y} - \mathbf{A}\mathbf{S}\|_F^2 + \lambda \|\mathbf{W} \odot \mathbf{S}\|_1 + \tau \|\mathbf{S}\|_{\text{HTV}} \\ \text{s.t. } \mathbf{A} \geq 0, \quad \mathbf{S} \geq 0, \quad \mathbf{1}_K^T \mathbf{S} = \mathbf{1}_N^T \quad (14)$$

where the first term is the standard fidelity term, parameter  $\lambda$  controls the sparsity of the abundance matrix, and the last term promotes the piecewise smoothness of the abundance maps.

Theoretically, the RSNMF model (8) is a special case of the TV-RSNMF model (14) when  $\tau$  is set to 0. Compared to the other NMF-based HU methods, there are two main improvements in TV-RSNMF. The first improvement is the introduction of the reweighted sparse regularizer into the NMF model, which is more effective than the  $L_1$  regularizer at promoting sparseness. The second improvement is that TV is used to denoise the abundance maps, which can explicitly explore the piecewise smooth structure of HSI data. Next, we introduce the solution to the proposed model.

#### IV. MODEL OPTIMIZATION AND PARAMETER SETTING FOR TV-RSNMF

Clearly, the TV-RSNMF model (14) is nonconvex with respect to  $\mathbf{A}$  and  $\mathbf{S}$ . To efficiently solve the problem, we introduce an auxiliary variable  $\mathbf{L}$  and convert (14) into the following equivalent problem:

$$J(\mathbf{A}, \mathbf{S}, \mathbf{L}) = \min_{\mathbf{A}, \mathbf{S}, \mathbf{L}} \frac{1}{2} \|\mathbf{Y} - \mathbf{A}\mathbf{S}\|_F^2 + \lambda \|\mathbf{W} \odot \mathbf{S}\|_1 + \tau \|\mathbf{L}\|_{\text{HTV}} \\ \text{s.t. } \mathbf{A} \geq 0, \quad \mathbf{S} \geq 0, \quad \mathbf{L} = \mathbf{S}, \quad \mathbf{1}_K^T \mathbf{S} = \mathbf{1}_N^T.$$

If we consider  $\mathbf{S}$  as the noisy version of the auxiliary variable  $\mathbf{L}$ , then the constraint  $\mathbf{L} = \mathbf{S}$  can be absorbed into the objective function, and we obtain the following alternative relaxation problem:

$$J(\mathbf{A}, \mathbf{S}, \mathbf{L}) = \min_{\mathbf{A}, \mathbf{S}, \mathbf{L}} \frac{1}{2} \|\mathbf{Y} - \mathbf{A}\mathbf{S}\|_F^2 + \lambda \|\mathbf{W} \odot \mathbf{S}\|_1 \\ + \frac{\mu}{2} \|\mathbf{L} - \mathbf{S}\|_F^2 + \tau \|\mathbf{L}\|_{\text{HTV}} \\ \text{s.t. } \mathbf{A} \geq 0, \quad \mathbf{S} \geq 0, \quad \mathbf{1}_K^T \mathbf{S} = \mathbf{1}_N^T \quad (15)$$

where parameter  $\mu$  acts as the penalty parameter and controls the similarity between the abundance matrix  $\mathbf{S}$  and the variable  $\mathbf{L}$ . Subsequently, a multiplicative iterative method [42] is adopted to solve problem (15), which splits the optimization of (15) into the following three subproblems:

$$\mathbf{A} = \arg \min_{\mathbf{A}} J(\mathbf{A}, \mathbf{S}, \mathbf{L}) \quad (16a)$$

$$\mathbf{S} = \arg \min_{\mathbf{S}} J(\mathbf{A}, \mathbf{S}, \mathbf{L}) \quad (16b)$$

$$\mathbf{L} = \arg \min_{\mathbf{L}} J(\mathbf{A}, \mathbf{S}, \mathbf{L}). \quad (16c)$$

The proposed method consists of three steps: 1) an endmember estimation step; 2) an abundance estimation step; and 3) an abundance denoising step. In each step, one variable is updated conditionally upon the current value of the other variables, such that the value of the objective function decreases iteratively. A more detailed description is presented in the following.

#### A. Update Rules

1) *Endmember Estimation*: The objective minimization function to estimate the endmembers is formulated as follows:

$$J(\mathbf{A}) = \min_{\mathbf{A}} \frac{1}{2} \|\mathbf{Y} - \mathbf{A}\mathbf{S}\|_F^2 + \text{Tr}(\Psi\mathbf{A}). \quad (17)$$

In (17), we add the nonnegative constraint to the objective function, and  $\Psi \in \mathbf{R}^{L \times K}$  is the Lagrange multiplier in matrix format. To find the minima of (17), one intuitive approach is to differentiate (17) and set the partial derivatives to 0. Based on the Karush–Kuhn–Tucker (K-K-T) conditions, we obtain the following linear equations:

$$\nabla_{\mathbf{A}} J(\mathbf{A}) = \mathbf{A}\mathbf{S}\mathbf{S}^T - \mathbf{Y}\mathbf{S}^T + \Psi = \mathbf{0} \quad (18a)$$

$$\mathbf{A} \odot \Psi = \mathbf{0}. \quad (18b)$$

By element-wise multiplication of both sides of (18a) with  $\mathbf{A}$ , we can obtain the following equation:

$$\mathbf{A} \odot (\mathbf{A}\mathbf{S}\mathbf{S}^T) - \mathbf{A} \odot (\mathbf{Y}\mathbf{S}^T) + \mathbf{A} \odot \Psi = \mathbf{0}. \quad (19)$$

Substituting (18b) into (19), we obtain the endmember update rule

$$\mathbf{A} \leftarrow \mathbf{A} \odot (\mathbf{Y}\mathbf{S}^T) \oslash (\mathbf{A}\mathbf{S}\mathbf{S}^T). \quad (20)$$

in which  $\oslash$  represents the element-wise division.

2) *Abundance Estimation*: The second step (16b) is to estimate the abundance, the objective minimization function of which is formulated as

$$J(\mathbf{S}) = \min_{\mathbf{S}} \frac{1}{2} \|\mathbf{Y}_f - \mathbf{A}_f \mathbf{S}\|_F^2 + \lambda \|\mathbf{W} \odot \mathbf{S}\|_1 \\ + \frac{\mu}{2} \|\mathbf{L} - \mathbf{S}\|_F^2 + \text{Tr}(\Gamma\mathbf{S}) \quad (21)$$

where  $\mathbf{Y}_f$  and  $\mathbf{A}_f$  are augmented matrices

$$\mathbf{Y}_f = \begin{bmatrix} \mathbf{Y} \\ \delta \mathbf{1}_N^T \end{bmatrix}, \quad \mathbf{A}_f = \begin{bmatrix} \mathbf{A} \\ \delta \mathbf{1}_K^T \end{bmatrix}. \quad (22)$$

The Lagrange multiplier is of size  $\Gamma \in \mathbf{R}^{K \times N}$ , and the weighted matrix  $\mathbf{W}$  is estimated as shown in (9). Mathematically, the K-K-T conditions of the minimization (21) are presented as

$$\nabla_{\mathbf{S}} J(\mathbf{S}) = \mathbf{A}_f^T \mathbf{A}_f \mathbf{S} - \mathbf{A}_f^T \mathbf{Y}_f + \lambda \mathbf{W} + \mu (\mathbf{S} - \mathbf{L}) + \Gamma = \mathbf{0} \quad (23a)$$

$$\mathbf{S} \odot \Gamma = \mathbf{0}. \quad (23b)$$

Analogously, we also element-wise multiply both sides of (23a) with  $\mathbf{S}$ , and obtain the update rule

$$\mathbf{S} \leftarrow \mathbf{S} \odot (\mathbf{A}_f^T \mathbf{Y}_f + \mu \mathbf{L}) \oslash (\mathbf{A}_f^T \mathbf{A}_f \mathbf{S} + \lambda \mathbf{W} + \mu \mathbf{S}). \quad (24)$$

3) *Abundance Denoising*: In the third step, the TV regularized method is adopted to denoise the abundance maps presented in (16c), while also promoting the piecewise smooth structure of the abundance maps. The corresponding objective minimization function is as follows:

$$J(\mathbf{L}) = \min_{\mathbf{L}} \frac{\mu}{2} \|\mathbf{L} - \mathbf{S}\|_F^2 + \tau \|\mathbf{L}\|_{\text{HTV}} \quad (25)$$

which is equivalent to solving the following minimization problem:

$$J(\mathbf{L}) = \min_{\mathbf{L}} \sum_{j=1}^K \left( \frac{\mu}{2} \|\mathcal{F}\mathbf{L}^j - \mathcal{F}\mathbf{S}^j\|_F^2 + \tau \|\mathcal{F}\mathbf{L}^j\|_{\text{TV}} \right). \quad (26)$$

As a result, the abundance denoising step is divided into  $K$  standard TV denoising problems

$$\hat{\mathbf{L}}^j = \min_{\mathbf{L}^j} \frac{\mu}{2} \|\mathcal{F}\mathbf{L}^j - \mathcal{F}\mathbf{S}^j\|_F^2 + \tau \|\mathcal{F}\mathbf{L}^j\|_{\text{TV}}, \quad j = 1, \dots, K. \quad (27)$$

---

**Algorithm 2** Total Variation Regularized Reweighted Sparse NMF for HU

---

- 1 **Input:** The observed mixture data  $\mathbf{Y} \in \mathbf{R}^{L \times N}$ , the number of endmembers  $K$ , the parameters  $\lambda$ ,  $\tau$ ,  $\mu$ , and  $\delta$ .
  - 2 **Output:** Endmember signature matrix  $\mathbf{A}$  and abundance matrix  $\mathbf{S}$ .
  - 3 **Initialize**  $\mathbf{A}$ ,  $\mathbf{S}$ ,  $\mathbf{L}$ , and weighted matrix  $\mathbf{W}$ .
  - 4 **Repeat** until convergence:
    - 5 Update the weighted matrix with (9);
    - 6 Update  $\mathbf{A}$  by (20);
    - 7 Augment  $\mathbf{Y}$  and  $\mathbf{A}$  to obtain  $\mathbf{Y}_f$  and  $\mathbf{A}_f$ , respectively;
    - 8 Update  $\mathbf{S}$  by (24);
    - 9 Update  $\mathbf{L}$  by FGP.
- 

In this paper, we use the fast gradient projection algorithm introduced in [40] to solve problem (27).

Summarizing the aforementioned description, we arrive at a multiplicative iterative method to solve the TV-RSNMF model, as presented in Algorithm 2. In the Appendix, we prove that the objective function in (15) decreases monotonically at each iteration until convergence is reached.

### B. Initialization and Parameter Determination

Due to the global nonconvexity of the proposed TV-RSNMF, the initialization and parameter determination are important when implementing the proposed method. We give a detailed description of these issues in the following.

The first issue concerns the initialization of the endmember signature matrix  $\mathbf{A}$ , the abundance matrix  $\mathbf{S}$ , the auxiliary variable  $\mathbf{L}$ , and the weighted matrix  $\mathbf{W}$ . The auxiliary variable is set to  $\mathbf{L} = \mathbf{S}$ , and the weighted matrix is initialized as  $W_{i,j} := 1/(|\mathbf{S}_{i,j}| + \text{eps})$ . As a result, the main concern is the initialization of the endmember signature matrix  $\mathbf{A}$  and the abundance matrix  $\mathbf{S}$ . For the endmember matrix  $\mathbf{A}$ , there are generally two strategies: random initialization and selection from the original data. The former strategy randomly allocates values between 0 and 1 as entries of  $\mathbf{A}$ . The latter strategy consists of two methods. The first method is the spectral information divergence (SID)-based selection to determine  $\mathbf{A}$ , which was used in [25]. The second method is to utilize an unsupervised endmember extraction method to identify the endmembers as the input of  $\mathbf{A}$  [28]. After determining the endmember matrix  $\mathbf{A}$  in both methods, a fully constrained least-squares (FCLS) solution [15] is adopted to generate the abundance matrix  $\mathbf{S}$ .

The second issue we are concerned about here is the ANC and ASC constraints, which can reduce the solution space of the optimization. Generally, if the initial matrices  $\mathbf{A}$ ,  $\mathbf{S}$ , and  $\mathbf{L}$  are nonnegative, the update rules (20) and (24) can guarantee the nonnegativity of the matrices  $\mathbf{A}$  and  $\mathbf{S}$ . In addition, matrix  $\mathbf{L}$  can also remain nonnegative in the update rule (27), as introduced in [40]. The ASC constraint is controlled by parameter  $\delta$ , as shown in (22). A larger value of  $\delta$  can lead to a more accurate result, but with a much lower convergence rate. In order to achieve the desired tradeoff,  $\delta$  was selected as 15 in our experiments, as in [33].

The determination of parameters  $\lambda$ ,  $\tau$ , and  $\mu$  is also a vital issue for the proposed method. Parameter  $\mu$  is the penalty parameter for the violation of the linear constraint  $\mathbf{L} = \mathbf{S}$ . That is to say, the larger the value of  $\mu$ , the more the similar optimizations (14) and (15) are. We analyze the influence of parameter  $\mu$  on the HU results in the experimental part. From multiple experiments, we set  $\mu = 1e3$ . Parameter  $\lambda$  is dependent on the sparsity of matrix  $\mathbf{S}$ , and parameter  $\tau$  controls the impact of preserving the piecewise smooth structure of the abundance maps. However, the adaptive selection of these two parameters still remains an open problem, and we discuss the influence of the two parameters in the experimental part.

How to stop the updating is another important issue. Here, we adopt two stopping criteria for the optimization. The first criterion is to set an error tolerance that is predefined. Once the error is successively within the limits of the tolerance ten times, the iteration is stopped. The other criterion is to set a maximum iteration number, which was adopted in our experiments, using a maximum iteration number of 3000. Once either of these criteria is met, the optimization ends.

The last issue concerns the estimation of the endmember number. Even though this is important to the unmixing result, it is another independent topic. In the experiments, we assumed the number of endmembers to be known. In fact, the HySime method proposed in [43] could be adopted to estimate the number of endmembers.

## V. EXPERIMENTAL RESULTS AND DISCUSSION

Both synthetic and real-data experiments were undertaken to demonstrate the effectiveness of the proposed methods for HU. We compared the proposed TV-RSNMF and RSNMF methods with  $L_{1/2}$ -NMF [28], ASSNMF [30], graph regularized  $L_{1/2}$ -NMF (GLNMF) [33], and vertex component analysis/FCLS (VCA-FCLS) [12]. The results were evaluated using the spectral angle distance (SAD) and root-mean-square error (RMSE). The SAD was used to compare the similarity of the endmember signature  $\mathbf{A}_k$  and its estimate  $\hat{\mathbf{A}}_k$ , and is defined as

$$\text{SAD}_k = \arccos \left( \frac{\mathbf{A}_k^T \hat{\mathbf{A}}_k}{\|\mathbf{A}_k\| \|\hat{\mathbf{A}}_k\|} \right). \quad (28)$$

The RMSE is defined as

$$\text{RMSE}_k = \left( \frac{1}{N} \|\mathbf{S}_k - \hat{\mathbf{S}}_k\|^2 \right)^{1/2} \quad (29)$$

where  $\hat{\mathbf{S}}_k$  is the ground-truth abundance matrix for the  $k$ th endmember.

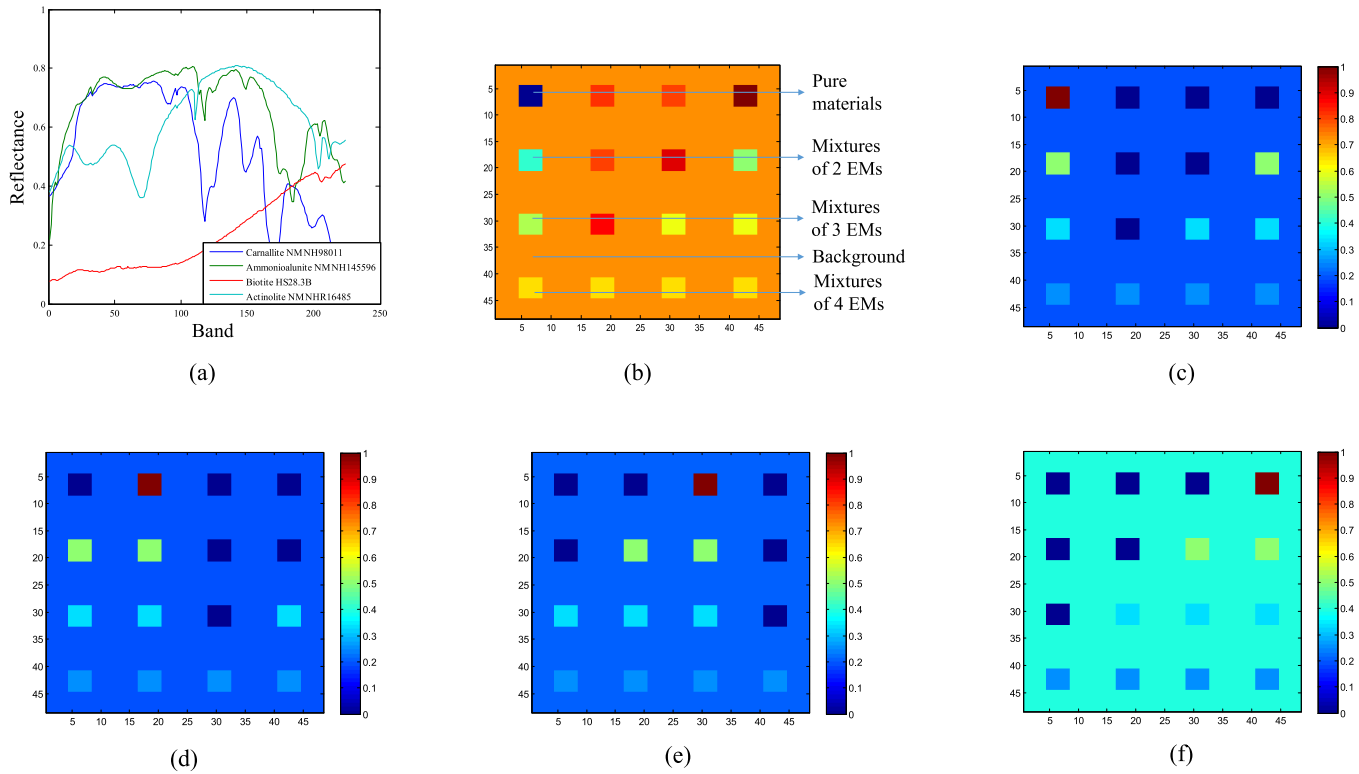


Fig. 3. True fractional abundances of endmembers in the simulated data cube. (a) Spectral signatures used to generate the simulated data. (b) Simulated image. Abundance map of (c) endmember 1, (d) endmember 2, (e) endmember 3, and (f) endmember 4.

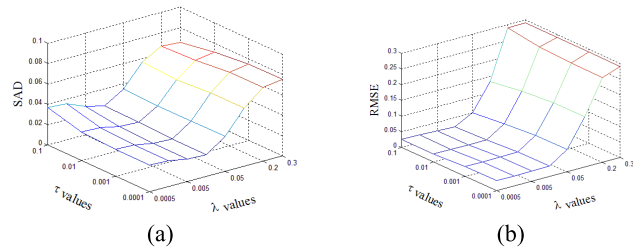


Fig. 4. Performance of TV-RSNMF with respect to parameters  $\lambda$  and  $\tau$  in terms of (a) SAD and (b) RMSE.

### A. Simulated Data Experiments

In the synthetic experiments, as shown in Fig. 3(a), four spectral signatures were chosen from the U.S. Geological Survey (USGS) digital spectral library,<sup>1</sup> which comprises spectral signatures with reflectance values given in 224 spectral bands, distributed uniformly in the interval  $0.4\text{--}2.5\ \mu\text{m}$ . Here, we only selected 187 low-noise bands to formulate the synthetic experiments, which was consistent with the subsequent real Airborne Visible/Infrared Imaging Spectrometer (AVIRIS) Cuprite data experiments. The simulated data, generated as described in [17], consisted of  $48 \times 48$  pixels and 187 bands per pixel. The data were generated using the LMM, with four signatures as the endmembers, imposing the ASC in each simulated pixel. Fig. 3(b) shows the simulated image. In the simulated image, there are pure regions as well as mixed regions constructed using mixtures ranging between

<sup>1</sup><http://speclab.cr.usgs.gov/spectral.lib>.

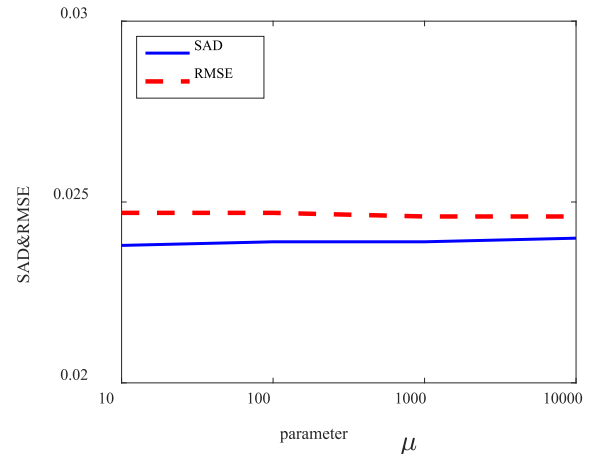


Fig. 5. Performance of TV-RSNMF with respect to parameter  $\mu$ .

two and four endmembers, distributed spatially in the form of distinct square regions. Fig. 3(c)–(f), respectively, shows the true fractional abundances for each of the four endmembers. The background pixels are also made up of mixtures of the same four endmembers, with different proportions. In addition, white Gaussian noise was added to the simulated data. The noise level was controlled by the SNR, which is denoted as

$$\text{SNR} = 10 \log_{10} \frac{E[x^T x]}{E[n^T n]} \quad (30)$$

where  $x$  and  $n$  represent the observation and noise of a pixel, respectively, and  $E[\cdot]$  denotes the expectation operator.

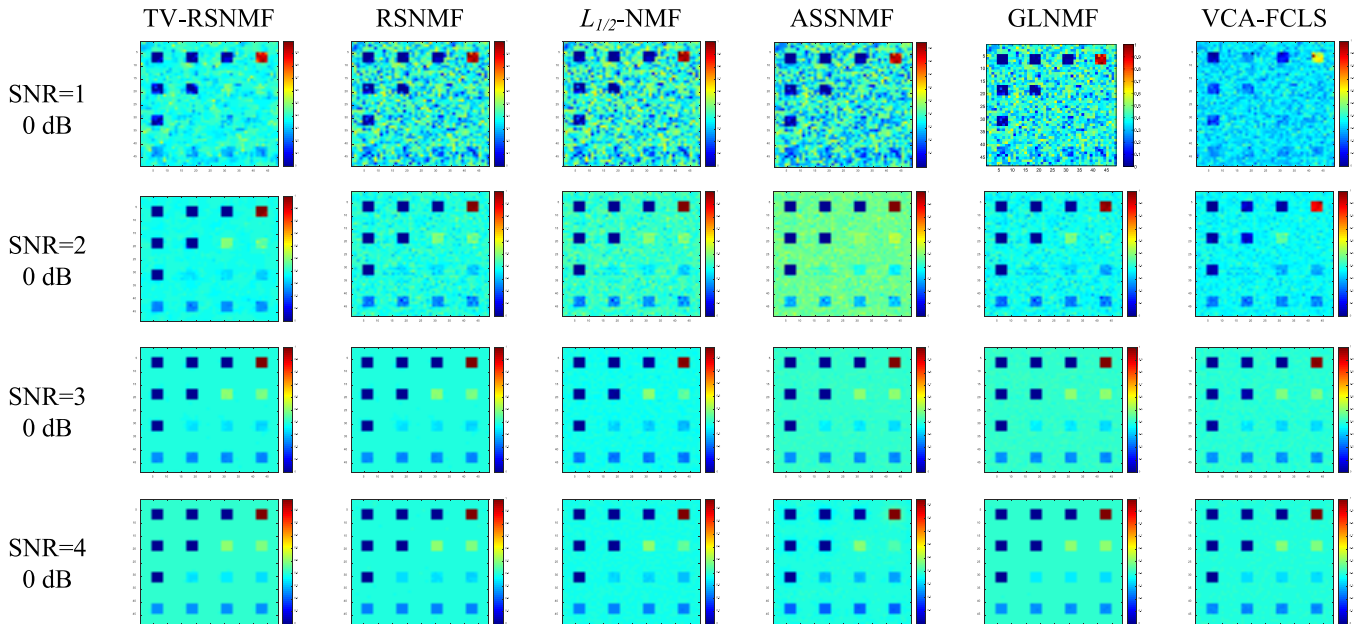


Fig. 6. Abundance maps obtained by the different unmixing methods for endmember 4 in the simulated data.

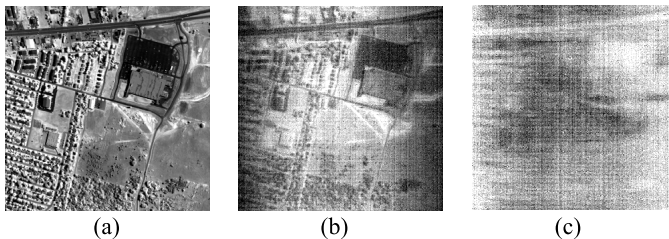


Fig. 7. Some bands of the HYDICE urban data set. (a) Low-noise band. (b) Noisy band. (c) Water-absorption band.

To allow a fair comparison, in all the simulated experiments, the initial endmember matrix was fixed and was the same as the SID result, and the initial abundance maps were generated by FCLS.

1) *Parameter Analysis*: We first present the influence of the sparse regularization parameter  $\lambda$  and the TV regularization parameter  $\tau$  on the unmixing results of the simulated data, for the case of SNR = 20 dB. The proposed TV-RSNMF method was tested using different values of parameters  $\lambda$  and  $\tau$ . In the experiments,  $\lambda$  was changed from  $5e-4$ ,  $1e-3$ ,  $5e-3$ , 0.01, 0.05, 0.1, 0.2, to 0.3, and  $\tau$  was changed from  $1e-4$ ,  $1e-3$ , 0.01, to 0.1. Parameter  $\mu$  was fixed as  $1e3$ . All possible combinations of these parameters were considered. Fig. 4(a) shows the SAD results achieved by TV-RSNMF with the different values of parameters  $\lambda$  and  $\tau$ , and Fig. 4(b) shows the RMSE results. From the figures, it can be observed that the SAD and RMSE values are stable and robust when the two parameters have relatively low values. However, when the two parameters are close to 0, the SAD and RMSE values increase. This indicates the positive influence of the two regularizers with the proper selection of parameters  $\lambda$  and  $\tau$ . Due to the high stability of parameter  $\tau$ , we set its value as 0.01 in all the experiments. The value of parameter  $\lambda$  is related to the sparsity of the abundance maps. Qian *et al.* [28] provided a

method to estimate the sparse regularization parameter  $\lambda$  as follows:

$$\lambda_e = \frac{1}{\sqrt{L}} \sum_{l=1}^N \frac{\sqrt{N} - \|\mathbf{Y}_l\|_1 / \|\mathbf{Y}_l\|_2}{\sqrt{N} - 1}. \quad (31)$$

From Fig. 4, it can be seen that the optimal parameter  $\lambda$  in the proposed TV-RSNMF method is smaller than  $\lambda_e$ . To sum up, it is recommended that parameter  $\lambda$  of the TV-RSNMF and RSNMF algorithms is selected from the range  $[\lambda_e/10, \lambda_e]$ . In the following simulated experiments, parameter  $\lambda$  of the TV-RSNMF and RSNMF algorithms was set as 0.01.

Subsequently, we present the influence of the sparse regularization parameter  $\mu$  on the unmixing results of the simulated data, for the case of SNR = 20 dB. In the experiments, parameter  $\mu$  was changed from  $1e1$ ,  $1e2$ ,  $1e3$ , to  $1e4$ , with the other parameters fixed. The SAD results achieved by TV-RSNMF with the different values of parameter  $\mu$  are reported in Fig. 5. From Fig. 5, it can be clearly observed that the proposed TV-RSNMF is quite robust to parameter  $\mu$ , inspiring us to fix parameter  $\mu$  as  $1e3$  in all our experiments.

2) *Performance Comparisons*: We also present the unmixing results with the simulated data contaminated by different levels of white Gaussian noise. The noise level was selected as SNR = 10, 20, 30, and 40 dB, respectively. Table I shows the SAD results achieved by the different methods with the simulated data sets using all the considered SNR levels, and Table II presents the RMSE results. In the tables, the best results are labeled in bold, and the second-best results are underlined. From Tables I and II, it can be clearly observed that RSNMF achieves lower SAD and RMSE values than  $L_{1/2}$ -NMF, ASSNMF, GLNMF, and VCA-FCLS. This indicates the advantage of the reweighted sparse regularizer in the NMF model. In addition, for RMSE, TV-RSNMF obtains better results than those of RSNMF. When the simulated data

TABLE I  
SAD VALUES OF THE DIFFERENT METHODS WITH THE SIMULATED DATA

Method	TV-RSNMF	RSNMF	$L_{1/2}$ -NMF	ASSNMF	GLNMF	VCA-FCLS
SNR=10 dB	<b>0.0452</b>	0.0492	0.0525	0.0627	<u>0.0460</u>	0.0751
SNR=20 dB	<b>0.0230</b>	<u>0.0248</u>	0.0257	0.0283	0.0314	0.0374
SNR=30 dB	<b>0.0091</b>	<u>0.0094</u>	0.0157	0.0152	0.0147	0.0297
SNR=40 dB	<u>0.0060</u>	<b>0.0047</b>	0.0141	0.0130	0.0089	0.0196

TABLE II  
RMSE VALUES OF THE DIFFERENT METHODS WITH THE SIMULATED DATA

Method	TV-RSNMF	RSNMF	$L_{1/2}$ -NMF	ASSNMF	GLNMF	VCA-FCLS
SNR=10 dB	<b>0.0496</b>	0.0774	0.0910	0.0818	<u>0.0771</u>	0.0919
SNR=20 dB	<b>0.0213</b>	<u>0.0328</u>	0.0417	0.0522	0.0491	0.0625
SNR=30 dB	<b>0.0129</b>	0.0168	0.0224	0.0330	0.0198	<u>0.0137</u>
SNR=40 dB	<b>0.0051</b>	<u>0.0109</u>	0.0207	0.0256	0.0134	0.0112

TABLE III  
SAD VALUES OF THE DIFFERENT METHODS WITH THE REAL URBAN DATA SET

Method	TV-RSNMF	RSNMF	$L_{1/2}$ -NMF	ASSNMF	GLNMF	VCA-FCLS
Asphalt road	<u>0.0944</u>	<b>0.0933</b>	0.1046	0.1772	0.1054	0.2903
Grass	<b>0.1165</b>	<u>0.1182</u>	0.1206	0.1663	0.1205	0.4906
Concrete road	<u>0.0630</u>	0.0656	<b>0.0609</b>	0.1034	0.0686	0.1887
Roof#1	<b>0.1229</b>	<u>0.1270</u>	0.1364	0.1594	0.1339	0.4008
Roof#2	<b>0.1553</b>	<u>0.1750</u>	0.2363	0.3291	0.2397	0.5268
Tree	<b>0.0613</b>	<u>0.0642</u>	0.0857	0.2238	0.0836	0.2722
Mean	<b>0.1022</b>	<u>0.1073</u>	0.1241	0.1932	0.1253	0.3616

are contaminated with a high noise level, the advantage is more obvious. This phenomenon demonstrates the superiority of the TV regularizer with the noisy data. From another aspect, the SAD value of RSNMF is slightly lower than that of TV-RSNMF in the case of an SNR of 40 dB. This is mainly due to the fact that the TV regularizer aims to explore the piecewise smooth structure of the abundance maps, ignoring the structural exploration of the endmembers.

To further display the performance of the different methods, we also show the abundance maps estimated for one randomly selected endmember, considering different noise levels, in the simulated data. Fig. 6 presents the results obtained for endmember 4. From the figure, it can be clearly observed that TV-RSNMF achieves smoother abundance maps than the other methods, no matter the level of noise. Notably, in the case of SNR = 20 dB, the background part of the abundance map extracted by TV-RSNMF is homogeneous over the whole image. Meanwhile, the backgrounds of the abundance maps extracted by the other methods are all contaminated by noise. As reported above, the TV regularizer, which indicates one kind of spatial processing, is extremely useful in HU when the SNR is low.

### B. Real-Data Experiments

Two real-world HSI data sets were used to conduct real-data experiments: the Hyperspectral Digital Imagery Collection Experiment (HYDICE) urban data set and the AVIRIS Cuprite data set. For all the methods implemented in the real-data experiments, we used the SID-based method to select pixels as the initial endmember matrix. The initial endmember matrix

was the same for all the NMF-based unmixing methods with the same real data set, and the experiments were repeated ten times, to ensure a reliable comparison. Parameters  $\tau$  and  $\mu$  were set as 0.01 and 1e3, respectively, and parameter  $\lambda$  was set as 0.2, which was within the range of  $[\lambda_e/10, \lambda_e]$ , and  $\lambda_e$  was estimated by (31).

1) *HYDICE Urban Data Set*: The original urban data set contains 210 bands that cover the wavelength range of 400–2500 nm. Fig. 7 shows some bands of the original data, which include low-noise bands, noisy bands, and water-absorption bands. In the experiment, noisy bands and water-absorption bands (bands 1–4, 76, 87, 101–111, 136–153, and 198–210) were removed before the unmixing, leaving 162 bands in total. In light of the previous analyses [28], [30], [44], six types of signatures named “Asphalt,” “Grass,” “Concrete road,” “Roof#1,” “Roof#2,” and “Tree” were estimated in the image. The reference signatures were collected from the spectral library which can be downloaded from.<sup>2</sup>

Table III gives the mean SAD values obtained by the different HU methods, to present the quantitative evaluation. From the table, it can be clearly observed that the proposed TV-RSNMF and RSNMF methods achieve lower mean SAD values than the other methods. This demonstrates the superiority of the proposed reweighted sparse regularizer. In addition, TV-RSNMF performs slightly better than RSNMF, which indicates that the spatial processing by the use of the TV regularizer is effective, even when we omit the high-noise

<sup>2</sup><http://www.agc.army.mil/>

TABLE IV  
SAD VALUES OF THE DIFFERENT METHODS WITH THE REAL CUPRITE DATA SET

Method	TV-RSNMF	RSNMF	$L_{1/2}$ -NMF	ASSNMF	GLNMF	VCA-FCLS
Alunite	<b>0.1930</b>	<u>0.2013</u>	0.2305	0.2380	0.2030	0.2045
Andradite	<u>0.0711</u>	0.0745	<b>0.0673</b>	0.0750	0.0821	0.0716
Buddingtonite	<u>0.1059</u>	0.1160	0.1117	<b>0.1015</b>	0.1189	0.1161
Dumortierite	<b>0.0959</b>	<u>0.0988</u>	0.1230	0.1173	0.1081	0.1031
Kaolinite_1	<u>0.0963</u>	0.0999	0.1025	0.1360	0.1480	<b>0.0871</b>
Kaolinite_2	<u>0.0740</u>	<b>0.0728</b>	0.0968	0.1374	0.0922	0.0821
Muscovite	<u>0.1306</u>	<b>0.1194</b>	0.1516	0.1434	0.1479	0.1472
Montmorillonite	0.0616	<u>0.0611</u>	0.0635	<b>0.0601</b>	0.0697	0.1070
Nontronite	0.0784	<u>0.0782</u>	0.0824	0.0864	<b>0.0781</b>	0.07882
Pyrope	<b>0.0610</b>	0.0871	0.0809	0.1267	0.0541	<u>0.0745</u>
Sphene	0.1099	<u>0.0956</u>	0.1168	0.2490	0.1005	<b>0.0889</b>
Chalcedony	<u>0.0988</u>	<b>0.0916</b>	0.1315	0.1045	0.1218	0.1327
Mean	<b>0.0981</b>	<u>0.0997</u>	0.1132	0.1313	0.1104	0.1078

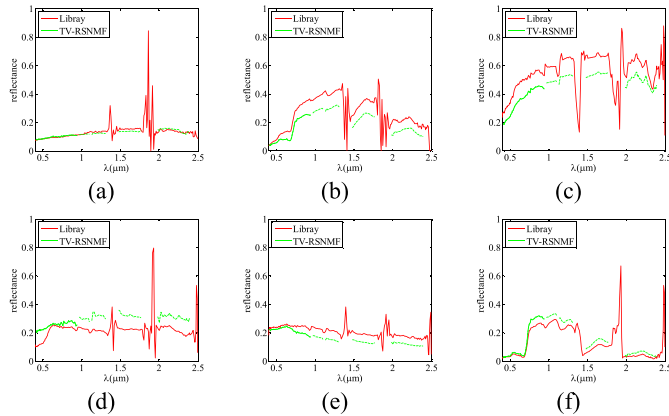


Fig. 8. Comparison of the library spectra with the endmember signatures extracted by TV-RSNMF on the urban data set. (a) Asphalt road. (b) Grass. (c) Concrete road. (d) Roof#1. (e) Roof#2. (f) Tree.

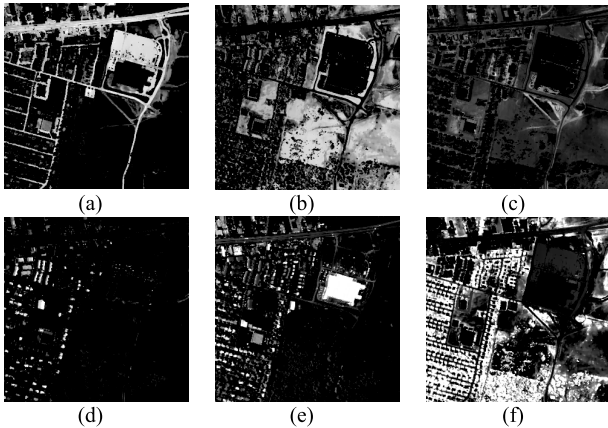


Fig. 9. Abundance maps of the different endmembers obtained using TV-RSNMF on the urban data set. (a) Asphalt road. (b) Grass. (c) Concrete road. (d) Roof#1. (e) Roof#2. (f) Tree.

and water-absorption bands before unmixing. We also present the unmixing results extracted by the TV-RSNMF method in one particular case of the experiments. Fig. 8 illustrates the endmember signatures extracted by TV-RSNMF and the reference signatures obtained from the library. Fig. 9 presents the grayscale abundance maps, where a dark pixel denotes a low abundance of the corresponding endmember.

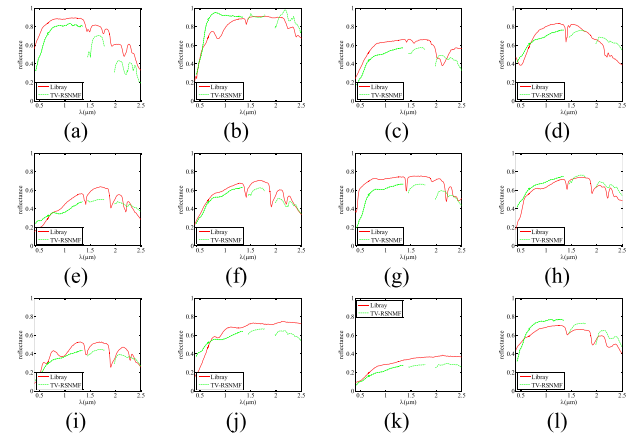


Fig. 10. Comparison between the USGS library spectra and the endmember signatures extracted by TV-RSNMF on the AVIRIS Cuprite data. (a) Alunite. (b) Andradite. (c) Buddingtonite. (d) Dumortierite. (e) Kaolinite\_1. (f) Kaolinite\_2. (g) Muscovite. (h) Montmorillonite. (i) Nontronite. (j) Pyrope. (k) Sphene. (l) Chalcedony.

2) *AVIRIS Cuprite Data Set*: The second HSI data set used in our real-data experiments was the AVIRIS Cuprite data set. The Cuprite data set contains 224 bands, which cover the wavelength range of 0.4–2.5  $\mu\text{m}$ . A total of 187 bands remained after removing the low-SNR and water-vapor absorption bands (bands 1–3, 104–113, 148–167, and 221–224). A spatial size of  $250 \times 191$  was tailored to conduct the unmixing procedure. The reference endmember signatures for the Cuprite data set were selected from the USGS digital spectral library, which was also utilized in [12] and [29].

According to the existing analysis in [12], there are 14 kinds of minerals in the Cuprite image. Since there are only tiny differences between some of the spectra of the same mineral with different chemical compositions, the estimated number of endmembers was reduced to 12 for the unmixing. Table IV presents the mean SAD values achieved by the different HU methods. From the table, it can again be clearly seen that the proposed methods achieve lower mean SAD values than the other methods. However, the advantage of the TV-RSNMF method over RSNMF is not so obvious. This is mainly because, in the Cuprite image, the abundance maps of some endmember signatures tend to be fragmentary, which weakens the influence of the TV regularizer. Fig. 10 presents

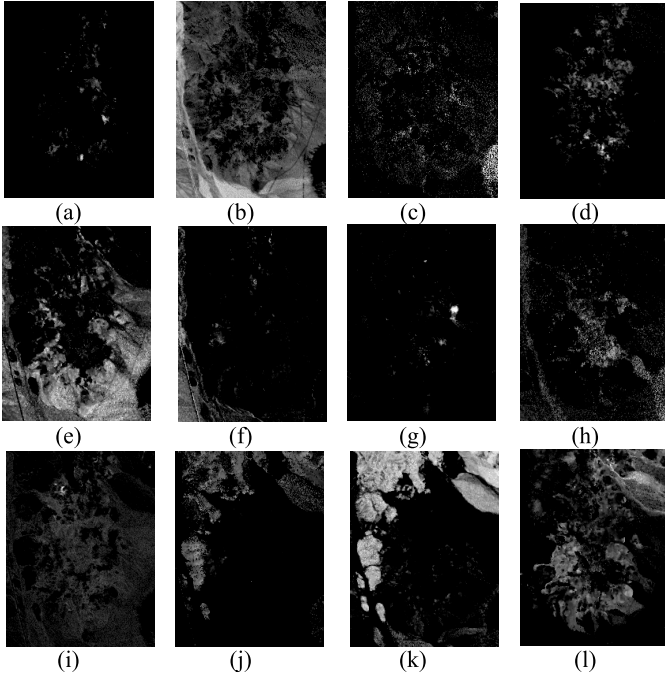


Fig. 11. Abundance maps of the different endmembers obtained using TV-RSNMF on the AVIRIS Cuprite data. (a) Alunite. (b) Andradite. (c) Buddingtonite. (d) Dumortierite. (e) Kaolinite\_1. (f) Kaolinite\_2. (g) Muscovite. (h) Montmorillonite. (i) Nontronite. (j) Pyrope. (k) Sphene. (l) Chalcedony.

the endmember signatures extracted by TV-RSNMF and the reference signatures obtained from the USGS library, and Fig. 11 shows the grayscale abundance maps. From the figures, it can be observed that the signatures extracted by TV-RSNMF are very similar to the reference signatures.

## VI. CONCLUSION

In this paper, we have proposed the TV-RSNMF method for blind HU. The TV-RSNMF model makes full use of the structure of the abundance maps to reduce the solution space of the NMF method. First, the weighted sparse regularizer is incorporated into the NMF model to enhance the sparseness of the abundance matrix. In this step, the weights of the weighted sparse regularizer are updated adaptively related to the abundance matrix of the current iteration. Second, the TV regularizer is adopted to denoise the abundance maps, resulting in the abundance maps being piecewise smooth. The proposed TV-RSNMF model is solved by a multiplicative iterative method, which consist of three steps: 1) endmember estimation; 2) abundance estimation; and 3) abundance denoising. The proposed method was compared with other state-of-the-art blind HU methods in several experiments, which confirmed the advantage of TV-RSNMF, in both visual and quantitative assessments.

Nevertheless, the proposed method still has room for improvement, and the adaptive selection of parameter  $\lambda$  remains a key problem. Moreover, in TV-RSNMF, we only explore the prior knowledge of the abundance maps, but prior knowledge of the endmembers is also important for NMF-based HU. How to effectively integrate the prior infor-

mation of both the abundance maps and endmembers into the NMF model will be the subject of our future work.

## APPENDIX

The objective function of TV-RSNMF is presented in (15). Our purpose here is to prove that this objective function is nonincreasing in each update step shown in Algorithm 2. That is to say, if we set  $\mathbf{A}^k, \mathbf{S}^k, \mathbf{L}^k$  as the values of the  $k$ th iteration and  $\mathbf{A}^{k+1}, \mathbf{S}^{k+1}, \mathbf{L}^{k+1}$  are the values obtained by the update rule presented in Algorithm 2, then we should prove

$$J(\mathbf{A}^{k+1}, \mathbf{S}^k, \mathbf{L}^k) \leq J(\mathbf{A}^k, \mathbf{S}^k, \mathbf{L}^k) \quad (32.a)$$

$$J(\mathbf{A}^{k+1}, \mathbf{S}^{k+1}, \mathbf{L}^k) \leq J(\mathbf{A}^{k+1}, \mathbf{S}^k, \mathbf{L}^k) \quad (32.b)$$

$$J(\mathbf{A}^{k+1}, \mathbf{S}^{k+1}, \mathbf{L}^{k+1}) \leq J(\mathbf{A}^{k+1}, \mathbf{S}^{k+1}, \mathbf{L}^k) \quad (32.c)$$

where the update rules are (20), (24), and (27), respectively. The inequality proof of (32.a) and (32.c) can be found in [28] and [40], respectively. We present the inequality proof of (32.b) as follows.

Since the objective function is separable in the columns of  $\mathbf{S}$ , we focus on each column of  $\mathbf{S}$  alone to prove the inequality of (32.b). The objective function then becomes

$$J(s) = \min \frac{1}{2} \|y - \mathbf{A}_f s\|_F^2 + \lambda \|w \odot s\|_1 + \frac{\mu}{2} \|l - s\|_F^2$$

$$\text{s.t. } s \geq 0, \quad \mathbf{1}_K^T s = \mathbf{1}_N^T \quad (33)$$

where  $y, s, w$ , and  $l$  are the column vectors of  $\mathbf{Y}, \mathbf{S}, \mathbf{W}$ , and  $\mathbf{L}$ , respectively. To prove the inequality, we introduce an auxiliary function  $G(s, s^k)$  [28] satisfying the conditions  $G(s, s) = J(s)$ ,  $G(s, s^k) \geq J(s)$ , and the following equation:

$$s^{k+1} = \arg \min G(s, s^k). \quad (34)$$

Thus, the inequality in each update is guaranteed by

$$J(s^{k+1}) \leq G(s^{k+1}, s^k) \leq G(s^k, s^k) = J(s^k). \quad (35)$$

Similar to [28], we define the auxiliary function  $G$  as

$$G(s, s^k) = J(s^k) + (s - s^k)(\nabla J(s^k))^T$$

$$+ \frac{1}{2}(s - s^k)K(s^k)(s - s^k)^T \quad (36)$$

where the diagonal matrix  $K(s^k)$  is

$$K(s^k) = \text{diag}((\mathbf{A}_f^T \mathbf{A}_f s^k + \lambda w + \mu s^k) \oslash s^k). \quad (37)$$

Note that the Taylor expansion of  $J(s)$  is

$$J(s) = J(s^k) + (s - s^k)(\nabla J(s^k))^T$$

$$+ \frac{1}{2}(s - s^k)(\mathbf{A}_f^T \mathbf{A}_f + \mu \mathbf{I})(s - s^k)^T + O(s) \quad (38)$$

where  $O(s)$  stands for the higher-order terms of the Taylor expansion. Thus, the condition  $G(s, s^k) \geq J(s)$  is satisfied if and only if

$$\frac{1}{2}(s - s^k)(K(s^k) - \mathbf{A}_f^T \mathbf{A}_f - \mu \mathbf{I})(s - s^k)^T \geq 0. \quad (39)$$

Due to the nonnegativity of  $s$  and  $w$ , the term  $K(s^k) - \mathbf{A}_f^T \mathbf{A}_f - \mu \mathbf{I}$  is easily identified as a positive semidefinite matrix [45]. It remains to be shown that the update rule

of (23) selects the minimum of  $G(s, s^k)$ . The minimum can be obtained by taking the gradient to be 0

$$\nabla_s G(s, s^k) = \mathbf{A}_f^T (\mathbf{A}_f s^k - y) + \lambda w + \mu (s^k - l) + K(s^k)(s - s^k) = 0. \quad (40)$$

By solving (40), we obtain

$$\begin{aligned} s &= s^k - K^{-1} (\mathbf{A}_f^T (\mathbf{A}_f s^k - y) + \lambda w + \mu (s^k - l)) \\ &= s^k - s^k \odot (\mathbf{A}_f^T \mathbf{A}_f s^k + \lambda w + \mu s^k) \\ &\quad \odot (\mathbf{A}_f^T (\mathbf{A}_f s^k - y) + \lambda w + \mu (s^k - l)) \\ &= s^k \odot (\mathbf{A}_f^T \mathbf{A}_f s^k + \lambda w + \mu s^k) \odot (\mathbf{A}_f^T y + \mu l) \end{aligned} \quad (41)$$

which is the desired update rule. This completes the proof.

#### ACKNOWLEDGMENT

The authors would like to thank the editor and the reviewers for their suggestions and comments, and Prof. J. M. Bioucas-Dias and Dr. F. Zhu for providing the reference spectra of the Cuprite data on their website.

#### REFERENCES

- [1] J. M. Bioucas-Dias *et al.*, "Hyperspectral unmixing overview: Geometrical, statistical, and sparse regression-based approaches," *IEEE J. Sel. Topics Appl. Earth Observat. Remote Sens.*, vol. 5, no. 2, pp. 354–379, Apr. 2012.
- [2] H. Zhang, W. He, L. Zhang, H. Shen, and Q. Yuan, "Hyperspectral image restoration using low-rank matrix recovery," *IEEE Trans. Geosci. Remote Sens.*, vol. 52, no. 8, pp. 4729–4743, Aug. 2014.
- [3] F. Melgani and L. Bruzzone, "Classification of hyperspectral remote sensing images with support vector machines," *IEEE Trans. Geosci. Remote Sens.*, vol. 42, no. 8, pp. 1778–1790, Aug. 2004.
- [4] D. W. J. Stein, S. G. Beaven, L. E. Hoff, E. M. Winter, A. P. Schaum, and A. D. Stocker, "Anomaly detection from hyperspectral imagery," *IEEE Signal Process. Mag.*, vol. 19, no. 1, pp. 58–69, Jan. 2002.
- [5] N. Keshava and J. F. Mustard, "Spectral unmixing," *IEEE Signal Process. Mag.*, vol. 19, no. 1, pp. 44–57, Jan. 2002.
- [6] H. Zhang, J. Li, Y. Huang, and L. Zhang, "A nonlocal weighted joint sparse representation classification method for hyperspectral imagery," *IEEE J. Sel. Topics Appl. Earth Observat. Remote Sens.*, vol. 7, no. 6, pp. 2056–2065, Jun. 2014.
- [7] H. Zhang, H. Zhai, L. Zhang, and P. Li, "Spectral–spatial sparse subspace clustering for hyperspectral remote sensing images," *IEEE Trans. Geosci. Remote Sens.*, vol. 54, no. 6, pp. 3672–3684, Jun. 2016.
- [8] W.-K. Ma *et al.*, "A signal processing perspective on hyperspectral unmixing: Insights from remote sensing," *IEEE Signal Process. Mag.*, vol. 31, no. 1, pp. 67–81, Jan. 2014.
- [9] N. Wang, B. Du, L. Zhang, and L. Zhang, "An abundance characteristic-based independent component analysis for hyperspectral unmixing," *IEEE Trans. Geosci. Remote Sens.*, vol. 53, no. 1, pp. 416–428, Jan. 2015.
- [10] N. Dobigeon, J.-Y. Tourneret, C. Richard, J. C. M. Bermudez, S. McLaughlin, and A. O. Hero, "Nonlinear unmixing of hyperspectral images: Models and algorithms," *IEEE Signal Process. Mag.*, vol. 31, no. 1, pp. 82–94, Jan. 2014.
- [11] J. Sigurdsson, M. O. Ulfarsson, and J. R. Sveinsson, "Hyperspectral unmixing with  $l_q$  regularization," *IEEE Trans. Geosci. Remote Sens.*, vol. 52, no. 11, pp. 6793–6806, Nov. 2014.
- [12] J. M. P. Nascimento and J. M. Bioucas-Dias, "Vertex component analysis: A fast algorithm to unmix hyperspectral data," *IEEE Trans. Geosci. Remote Sens.*, vol. 43, no. 4, pp. 898–910, Apr. 2005.
- [13] T.-H. Chan, C.-Y. Chi, Y.-M. Huang, and W.-K. Ma, "A convex analysis-based minimum-volume enclosing simplex algorithm for hyperspectral unmixing," *IEEE Trans. Signal Process.*, vol. 57, no. 11, pp. 4418–4432, Nov. 2009.
- [14] T.-H. Chan, W.-K. Ma, A. Ambikapathi, and C.-Y. Chi, "A simplex volume maximization framework for hyperspectral endmember extraction," *IEEE Trans. Geosci. Remote Sens.*, vol. 49, no. 11, pp. 4177–4193, Nov. 2011.
- [15] D. C. Heinz and C.-I. Chang, "Fully constrained least squares linear spectral mixture analysis method for material quantification in hyperspectral imagery," *IEEE Trans. Geosci. Remote Sens.*, vol. 39, no. 3, pp. 529–545, Mar. 2001.
- [16] M.-D. Iordache, J. Bioucas-Dias, and A. Plaza, "Sparse unmixing of hyperspectral data," *IEEE Trans. Geosci. Remote Sens.*, vol. 49, no. 6, pp. 2014–2039, Jun. 2011.
- [17] M.-D. Iordache, J. Bioucas-Dias, and A. Plaza, "Total variation spatial regularization for sparse hyperspectral unmixing," *IEEE Trans. Geosci. Remote Sens.*, vol. 50, no. 11, pp. 4484–4502, Nov. 2012.
- [18] X.-L. Zhao, F. Wang, T.-Z. Huang, M. K. Ng, and R. J. Plemmons, "Deblurring and sparse unmixing for hyperspectral images," *IEEE Trans. Geosci. Remote Sens.*, vol. 51, no. 7, pp. 4045–4058, Jul. 2013.
- [19] D. C. Zanotta, V. Haertel, Y. E. Shimabukuro, and C. D. Renno, "Linear spectral mixing model for identifying potential missing endmembers in spectral mixture analysis," *IEEE Trans. Geosci. Remote Sens.*, vol. 52, no. 5, pp. 3005–3012, May 2014.
- [20] D. D. Lee and H. S. Seung, "Learning the parts of objects by non-negative matrix factorization," *Nature*, vol. 401, no. 6755, pp. 788–791, Oct. 1999.
- [21] D. Donoho and V. Stodden, "When does non-negative matrix factorization give a correct decomposition into parts?" in *Proc. Adv. Neural Inf. Process. Syst.*, 2003, pp. 1141–1148.
- [22] V. P. Pauca, J. Piper, and R. J. Plemmons, "Nonnegative matrix factorization for spectral data analysis," *Linear Algebra Appl.*, vol. 416, no. 1, pp. 29–47, 2006.
- [23] L. Miao and H. Qi, "Endmember extraction from highly mixed data using minimum volume constrained nonnegative matrix factorization," *IEEE Trans. Geosci. Remote Sens.*, vol. 45, no. 3, pp. 765–777, Mar. 2007.
- [24] A. Huck, M. Guillaume, and J. Blanc-Talon, "Minimum dispersion constrained nonnegative matrix factorization to unmix hyperspectral data," *IEEE Trans. Geosci. Remote Sens.*, vol. 48, no. 6, pp. 2590–2602, Jun. 2010.
- [25] N. Wang, B. Du, and L. Zhang, "An endmember dissimilarity constrained non-negative matrix factorization method for hyperspectral unmixing," *IEEE J. Sel. Topics Appl. Earth Observat. Remote Sens.*, vol. 6, no. 2, pp. 554–569, Apr. 2013.
- [26] S. Jia and Y. Qian, "Constrained nonnegative matrix factorization for hyperspectral unmixing," *IEEE Trans. Geosci. Remote Sens.*, vol. 47, no. 1, pp. 161–173, Jan. 2009.
- [27] Z. Yang, G. Zhou, S. Xie, S. Ding, J.-M. Yang, and J. Zhang, "Blind spectral unmixing based on sparse nonnegative matrix factorization," *IEEE Trans. Image Process.*, vol. 20, no. 4, pp. 1112–1125, Apr. 2011.
- [28] Y. Qian, S. Jia, J. Zhou, and A. Robles-Kelly, "Hyperspectral unmixing via  $L_{1/2}$  sparsity-constrained nonnegative matrix factorization," *IEEE Trans. Geosci. Remote Sens.*, vol. 49, no. 11, pp. 4282–4297, Nov. 2011.
- [29] F. Zhu, Y. Wang, B. Fan, S. Xiang, G. Meng, and C. Pan, "Spectral unmixing via data-guided sparsity," *IEEE Trans. Image Process.*, vol. 23, no. 12, pp. 5412–5427, Dec. 2014.
- [30] X. Liu, W. Xia, B. Wang, and L. Zhang, "An approach based on constrained nonnegative matrix factorization to unmix hyperspectral data," *IEEE Trans. Geosci. Remote Sens.*, vol. 49, no. 2, pp. 757–772, Feb. 2011.
- [31] J. Liu, J. Zhang, Y. Gao, C. Zhang, and Z. Li, "Enhancing spectral unmixing by local neighborhood weights," *IEEE J. Sel. Topics Appl. Earth Observat. Remote Sens.*, vol. 5, no. 5, pp. 1545–1552, Oct. 2012.
- [32] F. Zhu, Y. Wang, S. Xiang, B. Fan, and C. Pan, "Structured sparse method for hyperspectral unmixing," *ISPRS J. Photogramm. Remote Sens.*, vol. 88, pp. 101–118, Feb. 2014.
- [33] X. Lu, H. Wu, Y. Yuan, P. Yan, and X. Li, "Manifold regularized sparse NMF for hyperspectral unmixing," *IEEE Trans. Geosci. Remote Sens.*, vol. 51, no. 5, pp. 2815–2826, May 2013.
- [34] E. J. Candes, M. B. Wakin, and S. P. Boyd, "Enhancing sparsity by reweighted  $l_1$  minimization," *J. Fourier Anal. Appl.*, vol. 14, no. 5, pp. 877–905, Dec. 2008.
- [35] W. He, H. Zhang, L. Zhang, W. Philips, and W. Liao, "Weighted sparse graph based dimensionality reduction for hyperspectral images," *IEEE Geosci. Remote Sens. Lett.*, vol. 13, no. 5, pp. 686–690, May 2016.
- [36] C. Y. Zheng, H. Li, Q. Wang, and C. L. P. Chen, "Reweighted sparse regression for hyperspectral unmixing," *IEEE Trans. Geosci. Remote Sens.*, vol. 54, no. 1, pp. 479–488, Jan. 2016.
- [37] W. He, H. Zhang, L. Zhang, and H. Shen, "Hyperspectral image denoising via noise-adjusted iterative low-rank matrix approximation," *IEEE J. Sel. Topics Appl. Earth Observat. Remote Sens.*, vol. 8, no. 6, pp. 3050–3061, Jun. 2015.

- [38] G. Martín and A. Plaza, "Spatial-spectral preprocessing prior to end-member identification and unmixing of remotely sensed hyperspectral data," *IEEE J. Sel. Topics Appl. Earth Observat. Remote Sens.*, vol. 5, no. 2, pp. 380–395, Apr. 2012.
- [39] L. I. Rudin, S. Osher, and E. Fatemi, "Nonlinear total variation based noise removal algorithms," *Phys. D, Nonlinear Phenomena*, vol. 60, nos. 1–4, pp. 259–268, 1992.
- [40] A. Beck and M. Teboulle, "Fast gradient-based algorithms for constrained total variation image denoising and deblurring problems," *IEEE Trans. Image Process.*, vol. 18, no. 11, pp. 2419–2434, Nov. 2009.
- [41] W. He, H. Zhang, L. Zhang, and H. Shen, "Total-variation-regularized low-rank matrix factorization for hyperspectral image restoration," *IEEE Trans. Geosci. Remote Sens.*, vol. 54, no. 1, pp. 178–188, Jan. 2016.
- [42] D. D. Lee and H. S. Seung, "Algorithms for non-negative matrix factorization," in *Proc. Adv. Neural Inf. Process. Syst.*, 2001, pp. 556–562.
- [43] J. M. Bioucas-Dias and J. M. P. Nascimento, "Hyperspectral subspace identification," *IEEE Trans. Geosci. Remote Sensing*, vol. 46, no. 8, pp. 2435–2445, Aug. 2008.
- [44] W. He, H. Zhang, and L. Zhang, "Sparsity-regularized robust non-negative matrix factorization for hyperspectral unmixing," *IEEE J. Sel. Topics Appl. Earth Observat. Remote Sens.*, vol. 9, no. 9, pp. 4267–4279, Sep. 2016.
- [45] P. O. Hoyer, "Non-negative sparse coding," in *Proc. 12th IEEE Workshop Neural Netw. Signal Process.*, Sep. 2002, pp. 557–565.



**Wei He** (S'14) received the B.S. degree from the School of Mathematics and Statistics, Wuhan University, Wuhan, China, in 2012, where he is currently pursuing the Ph.D. degree with the State Key Laboratory of Information Engineering in Surveying, Mapping and Remote Sensing.

His research interests include image quality improvement, remote sensing image processing, and low-rank representation.



**Hongyan Zhang** (M'13–SM'16) received the B.S. degree in geographic information system and the Ph.D. degree in photogrammetry and remote sensing from Wuhan University, Wuhan, China, in 2005 and 2010, respectively.

He has been an Associate Professor with the State Key Laboratory of Information Engineering in Surveying, Mapping and Remote Sensing, Wuhan University, since 2013. He has authored/co-authored more than 60 research papers. His research interests include image reconstruction for quality improvement, hyperspectral image processing, sparse representation, and low-rank methods for sensing image imagery.

Dr. Zhang is a reviewer for more than 20 international academic journals, including the IEEE TRANSACTIONS ON GEOSCIENCE AND REMOTE SENSING, the IEEE TRANSACTIONS ON IMAGE PROCESSING, the IEEE JOURNAL OF SELECTED TOPICS IN APPLIED EARTH OBSERVATIONS AND REMOTE SENSING, and the IEEE GEOSCIENCE AND REMOTE SENSING LETTERS.



**Liangpei Zhang** (M'06–SM'08) received the B.S. degree in physics from Hunan Normal University, Changsha, China, in 1982, the M.S. degree in optics from the Xi'an Institute of Optics and Precision Mechanics, Chinese Academy of Sciences, Xi'an, China, in 1988, and the Ph.D. degree in photogrammetry and remote sensing from Wuhan University, Wuhan, China, in 1998.

From 2011 to 2016, he was a Principal Scientist of the China State Key Basic Research Project, appointed by the Ministry of the National Science and Technology of China to lead the remote sensing program in China. He is currently the Head of the Remote Sensing Division, State Key Laboratory of Information Engineering in Surveying, Mapping and Remote Sensing, Wuhan University. He is also a Chang-Jiang Scholar Chair Professor appointed by the Ministry of Education of China. He has authored more than 500 research papers and five books, and holds 15 patents. He edited several conference proceedings, issues, and geoinformatics symposiums. His research interests include hyperspectral remote sensing, high-resolution remote sensing, image processing, and artificial intelligence.

Dr. Zhang is a Fellow of the Institution of Engineering and Technology and an Executive Member (Board of Governors) of the China National Committee of the International Geosphere-Biosphere Programme and the China Society of Image and Graphics. He received the 2010 Best Paper Boeing Award and the 2013 Best Paper ERDAS Award from the American Society of Photogrammetry and Remote Sensing, the Best Reviewer Awards from the IEEE Geoscience and Remote Sensing Society (GRSS) for his service to the IEEE JOURNAL OF SELECTED TOPICS IN APPLIED EARTH OBSERVATIONS AND REMOTE SENSING (JSTARS) in 2012 and the IEEE GEOSCIENCE AND REMOTE SENSING LETTERS in 2014. His research teams were a recipient of the top three prizes of the IEEE GRSS 2014 Data Fusion Contest, and his students have been selected as the winners or finalists of the IEEE International Geoscience and Remote Sensing Symposium Student Paper Contest in recent years. He was the General Chair of the Fourth IEEE GRSS Workshop on Hyperspectral Image and Signal Processing: Evolution in Remote Sensing and a Guest Editor of the IEEE JSTARS. He is the Founding Chair of the IEEE GRSS Wuhan Chapter. He serves as the Co-Chair of the series International Society for Optics and Photonics Conferences on Multispectral Image Processing and Pattern Recognition, the Conference on Asia Remote Sensing, and many other conferences. He also serves as an Associate Editor of the *International Journal of Ambient Computing and Intelligence*, the *International Journal of Image and Graphics*, the *International Journal of Digital Multimedia Broadcasting*, the *Journal of Geo-Spatial Information Science*, the *Journal of Remote Sensing*, and the IEEE TRANSACTIONS ON GEOSCIENCE AND REMOTE SENSING. He is a Guest Editor of the *Journal of Applied Remote Sensing* and the *Journal of Sensors*.